

Electronic structure of nickelate superconductor  $\text{NdNiO}_2\text{H}_x$  ( $x = 0, 0.25, 0.5$ ) under different strainsHangbo Qi,<sup>1</sup> Xuelei Sui,<sup>2</sup> Xiangru Han,<sup>2</sup> Bing Huang,<sup>2</sup> Haiyan Xiao,<sup>1,\*</sup> and Liang Qiao<sup>1,†</sup><sup>1</sup>*School of Physics, University of Electronic Science and Technology of China, Chengdu 611731, China*<sup>2</sup>*Beijing Computational Science Research Center, Beijing 100193, China*

(Received 31 January 2024; accepted 28 May 2024; published 11 June 2024)

The discovery of superconductivity in infinite-layer nickelates has drawn considerable attention and boosted numerous theoretical and experimental studies. Here, combining density functional theory and Wannier function calculations, we study the electronic structure of nickelate  $\text{NdNiO}_2\text{H}_x$  ( $x = 0, 0.25, 0.5$ ) (NNOH) under five different in-plane strains. We unveil that, with H introduced, the orbital occupation of Ni  $3d_{x^2-y^2}$  increases, accompanied by the shift of band structure toward lower energy under constant strain. Meanwhile, the H  $1s$  orbital hybridizes and forms a bonding-antibonding state with the Ni  $3d_{z^2}$  orbital, reducing the occupation of the Ni  $3d_{z^2}$  orbital, which results in the decreased filling of Ni  $3d$  orbital. By contrast, the strain has negligible influences on the filling of Ni  $3d$  and Ni  $e_g$  orbital polarization. As the H concentration increases, the contribution of the itinerant interstitial  $s$  (IIS) orbital to the band structure near the Fermi level gradually decreases and disappears at  $x = 0.5$  due to the doped H obliterating the IIS band. In addition, with compressive strain applied, the bandwidth of the Ni  $3d_{x^2-y^2}$  orbital increases, consistent with the calculated stronger effective Ni  $3d_{x^2-y^2}$  nearest-neighboring hopping. In addition, we find that the impact of H concentration and strain on the projected orbitals and calculated density of states is slight. Also, the influences of the Sr concentration (0–20%) and Hubbard  $U$  parameter on the electronic properties of NNO without strain are explored and found not to change the main conclusions.

DOI: [10.1103/PhysRevMaterials.8.064802](https://doi.org/10.1103/PhysRevMaterials.8.064802)

## I. INTRODUCTION

The cuprate Ba-La-Cu-O system as an unconventional superconductor was discovered by Bednorz and Müller [1] since its superconducting mechanism cannot be explained by the Bardeen-Cooper-Schrieffer (BCS) theory [2]. It exhibits high-temperature superconductivity with a transition temperature  $T_c \sim 30$  K. Subsequently, more cuprates with higher  $T_c$  such as  $\text{YBa}_2\text{Cu}_3\text{O}_7$  (95 K) [3],  $\text{Sr}_{1-y}\text{Nd}_y\text{CuO}_2$  (40 K) [4], and  $(\text{Sr}_{1-x}\text{Ca}_x)_{1-y}\text{CuO}_2$  (110 K) [5] were synthesized and studied. However, the underlying superconducting mechanism of cuprates has not been unveiled thus far. In recent years, the infinite-layer nickelate  $\text{Nd}_{0.8}\text{Sr}_{0.2}\text{NiO}_2$  superconductor as an analog of cuprates was reported by Li *et al.* [6] with a maximum transition temperature  $T_c \sim 15$  K, which provides a platform to investigate the unconventional superconductivity. After that, many theoretical and experimental studies were performed to explore the underlying superconducting mechanism of infinite-layer nickelates [7–12].

Infinite-layer nickelate  $\text{NdNiO}_2$  has a layered structure with alternating  $\text{NiO}_2$  and Nd layers, which is like other layered nickelates with an  $\text{NiO}_2$  plane, e.g.,  $\text{La}_3\text{Ni}_2\text{O}_6$  [13],  $\text{Nd}_4\text{Ni}_3\text{O}_8$  [14], and  $\text{Nd}_6\text{Ni}_5\text{O}_{12}$  [15]. These square-planar compounds are synthesized by chemical reduction, i.e., removal of the apical oxygen from the corresponding parent compounds. Specifically,  $\text{La}_3\text{Ni}_2\text{O}_6$  and  $\text{Nd}_{n+1}\text{Ni}_n\text{O}_{2n+2}$

( $n = 3$  or  $5$ ) are obtained via the reduction from Ruddlesden-Popper bilayer perovskite  $\text{La}_3\text{Ni}_2\text{O}_7$  and Ruddlesden-Popper  $\text{Nd}_{n+1}\text{Ni}_n\text{O}_{3n+1}$  ( $n = 3$  or  $5$ ) films, respectively. It should be noted that  $\text{NdNiO}_2$  is the infinite ( $n = \infty$ ) member of the broader layered  $\text{Nd}_{n+1}\text{Ni}_n\text{O}_{2n+2}$ .

The similarities and differences between nickelates and cuprates have been studied previously [16–18]. For example, Zhang *et al.* [17] investigated the structural, electronic, and magnetic properties of  $\text{NdNiO}_2/\text{SrTiO}_3$  (NNO/STO) and  $\text{CaCuO}_2/\text{SrTiO}_3$  (CCO/STO) systems based on density functional theory (DFT). They found that, for NNO/STO, there exists a two-dimensional (2D) electron gas at the interface due to the polar discontinuity, and it extends over several layers beyond the interface. For CCO/STO, the electronic rearrangement is very localized at the interface. Moreover, Botana and Norman [16] found that, in  $\text{LaNiO}_2$ , the large value of second- and third-neighbor hopping integrals and the  $e_g$  energy splitting of  $3d_{x^2-y^2}$  and  $3d_{z^2}$  are like those obtained in  $\text{CaCuO}_2$ , and Sr doping further increases the cuprate-like character of nickelates by suppressing the self-doping effect of the R  $5d$  bands. In addition, there is another remarkable difference between these two classes of materials, i.e., the infinite-layer nickelates are Mott-Hubbard insulators, while cuprates are charge-transfer insulators according to the Zaanen-Sawatzky-Allen (ZSA) scheme [19–22]. These differences and similarities show that the nickelate is a cupratelike unconventional superconductor, although its  $T_c$  is not as high as that of cuprates. In addition, the absence of superconductivity in bulk nickelates is a significant issue to be explained.

\*Contact author: [hyxiao@uestc.edu.cn](mailto:hyxiao@uestc.edu.cn)†Contact author: [liang.qiao@uestc.edu.cn](mailto:liang.qiao@uestc.edu.cn)

Generally, many physical characteristics like polar interface [23] and chemical composition [24] were found to be related to the superconductivity of nickelates. Based on DFT calculations Si *et al.* [25] proposed that the H intercalation has dramatic influences on the electronic structure and thus might be a reason why some nickelates are superconducting and others are not. Ding *et al.* [26] observed the zero-resistivity phenomenon in  $\text{Nd}_{0.8}\text{Sr}_{0.2}\text{NiO}_2\text{H}$  epitaxial films by introducing H in experiment. The obtained H-doping phase diagram corroborates that the  $\text{Nd}_{0.8}\text{Sr}_{0.2}\text{NiO}_2\text{H}_x$  exhibits superconductivity within a very narrow H-doping window of  $0.22 \leq x \leq 0.28$ , revealing the critical role of H in superconductivity. More interestingly, those layered nickelates  $\text{La}_3\text{Ni}_2\text{O}_6$ ,  $\text{Nd}_4\text{Ni}_3\text{O}_8$ , and  $\text{Nd}_6\text{Ni}_5\text{O}_{12}$  with apical oxygen deintercalation have been reported or predicted to exhibit superconductivity in the literature [27,28]. Considering this, H may also play a significant role in these compounds. Additionally, recent experiments show that the superconducting transition temperature of infinite-layer nickelates can be dramatically enhanced by 40% via only  $\sim 1\%$  compressive strain-tuning enabled by substrate design [29,30], which makes it possible for nickelates to be high-temperature superconductors. These phenomena indicate that the hydrogen and strain play significant roles in the superconductivity of nickelates. In this regard, it is indispensable to unambiguously ascertain the impact of these two factors on the physics of nickelates.

In this paper, we study the electronic structure of nickelate  $\text{NdNiO}_2\text{H}_x$  ( $x = 0, 0.25, 0.5$ ) (NNOH) under different in-plane strains to simulate the nickelate grown on six substrates [ $\text{SrTiO}_3$  (STO),  $\text{LaAlO}_3$  (LAO),  $(\text{LaAlO}_3)_{0.3}(\text{Sr}_2\text{TaAlO}_6)_{0.7}$  (LSAT),  $\text{NdGaO}_3$  (NGO),  $\text{GdScO}_3$  (GSO), and  $\text{DyScO}_3$  (DSO)] employing a DFT method combined with Wannier functions. As in prior work, three possible H sites are considered, and the total energies of corresponding structures are calculated. The results show that the structure with incorporated H located at the apical oxygen vacancy (AOV) position is energetically favorable. Then considering that the lattice constant of LSAT is the same as that of NGO, the  $2 \times 2 \times 2$  supercells of NNOH under five types of strains are constructed and optimized. Based on the relaxed structures, we investigate the density of states (DOSs), band structures, Mulliken gross orbital population (Mulliken GP), projected orbitals, and hopping between different orbitals in NNOH under different strains. The results show that introduced H obliterates the itinerant interstitial  $s$  (IIS) band near the Fermi level and hopping path to the IIS orbital, thus reducing the hybridization between Ni  $3d_{x^2-y^2}$  and IIS orbitals. Meanwhile, doping H enhances the filling of Ni  $3d_{x^2-y^2}$  and shifts the corresponding energy level to lower energy. Additionally, the strain is found to affect the bandwidth of the Ni  $3d_{x^2-y^2}$  orbital, i.e., the nearest-neighboring hopping is affected by the lattice strain.

## II. COMPUTATIONAL METHODS

In this paper, we perform first-principles calculations in the framework of DFT [31,32] as implemented in VASP [33] with the projector augmented-wave [34] method. The electron exchange-correlation potential is described using

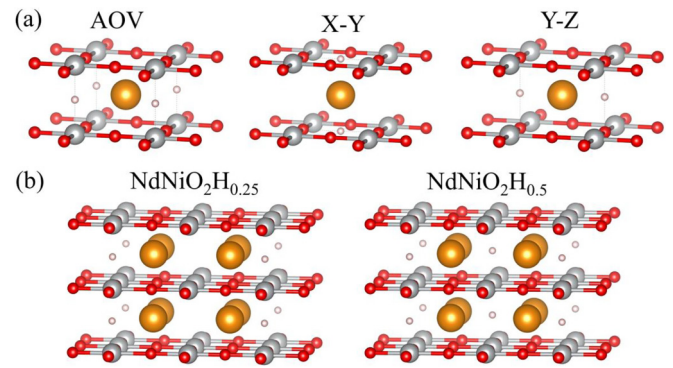


FIG. 1. Schematic configurations of (a) NNO unit cell with H located at three different sites and (b)  $2 \times 2 \times 2$  supercells of  $\text{NdNiO}_2\text{H}_x$  ( $x = 0.25, 0.5$ ). Brown: Nd; gray: Ni; red: O; white: H.

generalized gradient approximation as parametrized by the Perdew-Burke-Ernzerhof functional [35]. The cutoff energy is set to 600 eV. Here,  $k$ -point Monkhorst-Pack grids [36] of  $15 \times 15 \times 15$  and  $5 \times 5 \times 5$  are used for bulk NNO and  $2 \times 2 \times 2$  supercells of  $\text{NdNiO}_2\text{H}_x$  ( $x = 0.25, 0.5$ ), respectively. The atomic positions are optimized until the Hellman-Feynman forces and energy are  $< 10^{-2} \text{ eV/\AA}$  and  $10^{-6} \text{ eV}$ , respectively. Considering the inability of current DFT functionals to properly treat the localized  $4f$  electrons, we place the Nd  $4f$  electrons in the core [37]. In addition, to simulate the strain effects induced by different substrates, in-plane constants of the substrate are applied to the  $\text{NdNiO}_2\text{H}_x$  and fixed in the calculation. The maximally localized Wannier function (MLWF) [38] calculations are performed as implemented in WANNIER90 [39]. To fit the DFT-calculated band structures, we set 17 and 136 Wannier projectors for the NNO unit cell and  $\text{NdNiO}_2\text{H}_x$  ( $x = 0.25, 0.5$ ) supercells, respectively. Specifically, for the NNO unit cell, 5 Nd  $d$  orbitals, 5 Ni  $d$  orbitals, 6 O  $p$  orbitals, and an interstitial  $s$  orbital are used; for the  $\text{NdNiO}_2\text{H}_{0.25}$  supercell, 40 Nd  $d$  orbitals, 40 Ni  $d$  orbitals, 48 O  $p$  orbitals, 6 interstitial  $s$  orbitals, and 2 H  $s$  orbitals are used; and for the  $\text{NdNiO}_2\text{H}_{0.5}$  supercell, 40 Nd  $d$  orbitals, 40 Ni  $d$  orbitals, 48 O  $p$  orbitals, 4 interstitial  $s$  orbitals, and 4 H  $s$  orbitals are used. The outer and inner energy windows for the NNO unit cell are set to be  $[-36, 14 \text{ eV}]$  and  $[-8, 7 \text{ eV}]$ , respectively; for  $\text{NdNiO}_2\text{H}_x$  ( $x = 0.25, 0.5$ ) supercells, the outer and inner energy windows are set to be  $[-10, 18 \text{ eV}]$  and  $[-6, 5 \text{ eV}]$ , respectively.

## III. RESULTS AND DISCUSSIONS

### A. Geometrical structures of NNOH under different in-plane strains

In preliminary work, three configurations of NNOH with H located at different interstitial positions [i.e., the AOV, the center of the  $xy$  plane (X-Y), and the center of the  $yz$  plane (Y-Z)], as illustrated in Fig. 1(a), are constructed and optimized. The total energies are calculated to be  $-31.71 \text{ eV}$  (AOV),  $-28.33 \text{ eV}$  (X-Y), and  $-29.20 \text{ eV}$  (Y-Z), suggesting that the NNOH with H located at the AOV position is the most stable configuration. This is consistent with the results reported by Ding *et al.* [26]. In this regard, we

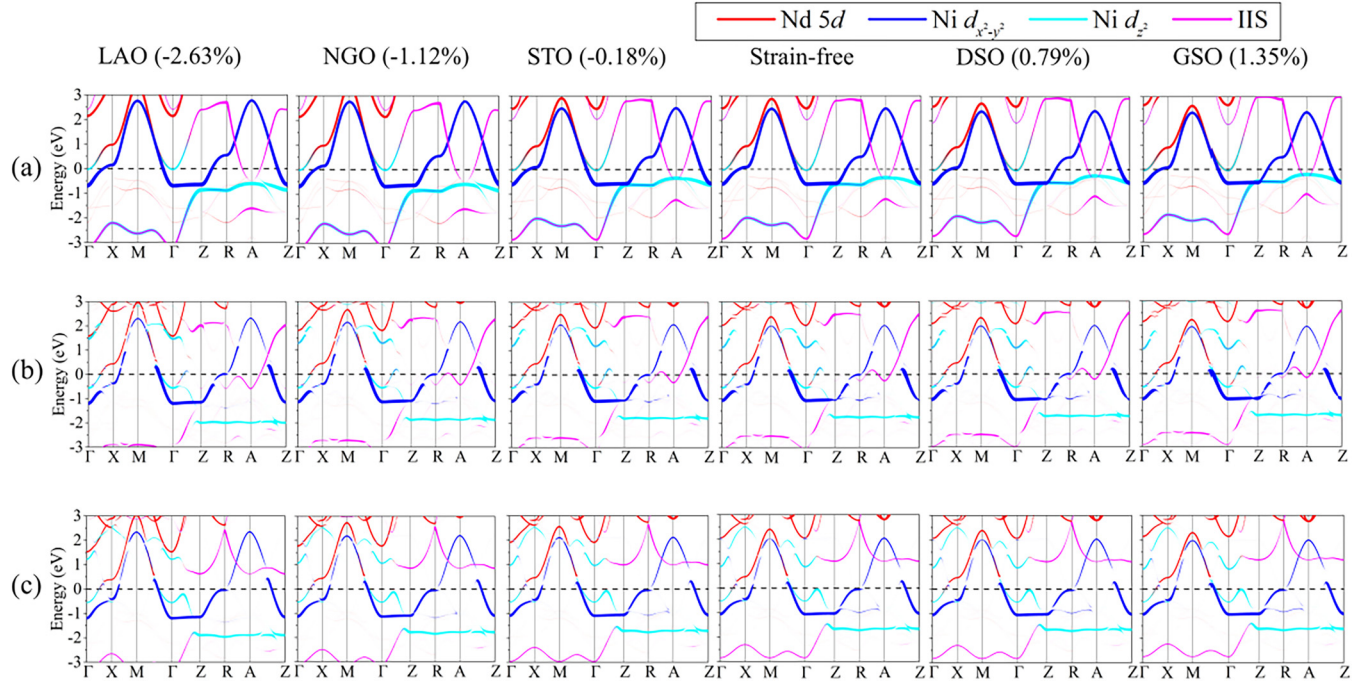


FIG. 2. Projected band structures of  $\text{NdNiO}_2\text{H}_x$  [(a)  $x = 0$ , (b)  $x = 0.25$ , and (c)  $x = 0.5$ ] under different strains. The Fermi level has been set to 0 eV.

focus on the AOV configuration to construct the supercells with H intercalation, as shown in Fig. 1(b). Additionally, five types of in-plane strains are considered to simulate NNOH grown on STO, LAO, LSAT/NGO, GSO, and DSO substrates. Considering that the in-plane lattice constant of NNO is 3.912 Å, the compressive strains of 2.63, 1.12, and 0.18% corresponding to the lattice constants of LAO (3.809 Å), LSAT/NGO (3.868 Å), and STO (3.905 Å) are applied, respectively. Likewise, the tensile strains of 0.79 and 1.35% corresponding to the lattice constants of DSO (3.943 Å) and GSO (3.965 Å) are applied, respectively. In the literature, a similar method has been employed to simulate nickelate films grown on different perovskite substrates [40–42].

### B. Electronic structures of NNOH under different in-plane strains

To understand the electronic structure evolution induced by H intercalation and interface stress, we calculate the band structures and DOS of  $\text{NdNiO}_2\text{H}_x$  ( $x = 0, 0.25, 0.5$ ) under different in-plane strains. The band structures are plotted in Figs. 2(a)–2(c). Considering that the contribution of band structures for Ni  $t_{2g}$  in bulk NNO near the Fermi level are negligible [43], we do not put them in the band structures. As compared with the case without H doping [see Fig. 2(a)], the energy level of Ni  $3d_{x^2-y^2}$  shifts to lower energy under each strain after introducing H [see Figs. 2(b) and 2(c)], indicating that the Ni  $3d_{x^2-y^2}$  orbital basically gains electrons, as will be further discussed in Sec. III C. In addition, with the increasing H concentration, the energy level of the IIS band near the Fermi level gradually decreases and eventually disappears. Moreover, with compressive strain being applied, the bandwidth of the Ni  $3d_{x^2-y^2}$  orbital increases in all

cases. For example, the bandwidth of the Ni  $3d_{x^2-y^2}$  orbital in NNO [Fig. 2(a)] increases from 3.04 eV (strain-free state) to 3.43 eV under 2.63% compressive strain. This phenomenon suggests that the effective Ni  $3d_{x^2-y^2}$  nearest-neighbor hopping becomes stronger [44,45], which will be further discussed in Sec. III D, whereas under tensile strain, the band structure of  $\text{NdNiO}_2\text{H}_x$  ( $x = 0, 0.25, 0.5$ ) shows negligible changes, which indicates that tensile strain has slight influences on the electronic structures of NNOH.

Figures 3(a)–3(c) shows the projected DOS (PDOS) for IIS and H  $1s$  orbitals and total DOS (TDOS) in NNOH under different strains. In all cases, the DOSs under different H concentrations are like each other, suggesting that both the PDOSs and TDOSs are insensitive to the H concentration. As for the case under different strains, the TDOSs and PDOSs for the H  $1s$  orbital are almost unchanged, i.e., they are hardly affected by the strain. Notably, the DOSs of the occupied  $1s$  state for H in NNOH are much larger than the unoccupied part, indicating that the valance state of H is negative [26]. In addition, there is a slight band shift in the PDOSs for the IIS orbital of  $\text{NdNiO}_2\text{H}_x$  ( $x = 0, 0.25, 0.5$ ) under different strains. For example, in the PDOSs for IIS of NNO, the peak without in-plane strain shifts from  $-2.2$  to  $-2.4$  eV under LAO in-plane strain. The subsequent calculations of crystal orbital Hamilton populations (COHPs) [46,47] confirm that the Mulliken GP [48] of H in NNOH is  $\sim 1.7$ , suggesting that the valance state of H is about  $-0.7$ , which is consistent with experimental results of H-doped transition-metal oxides deintercalated using topotactic reduction [49–51]. In addition, the Fermi energy of NNO under each strain has been summarized in Table I. It is noted that the Fermi level shifts to higher energy under compressive strains (LAO, NGO, and STO in-plane strains), indicative of an  $n$ -type doping effect. Conversely, the Fermi level shifts to lower energy

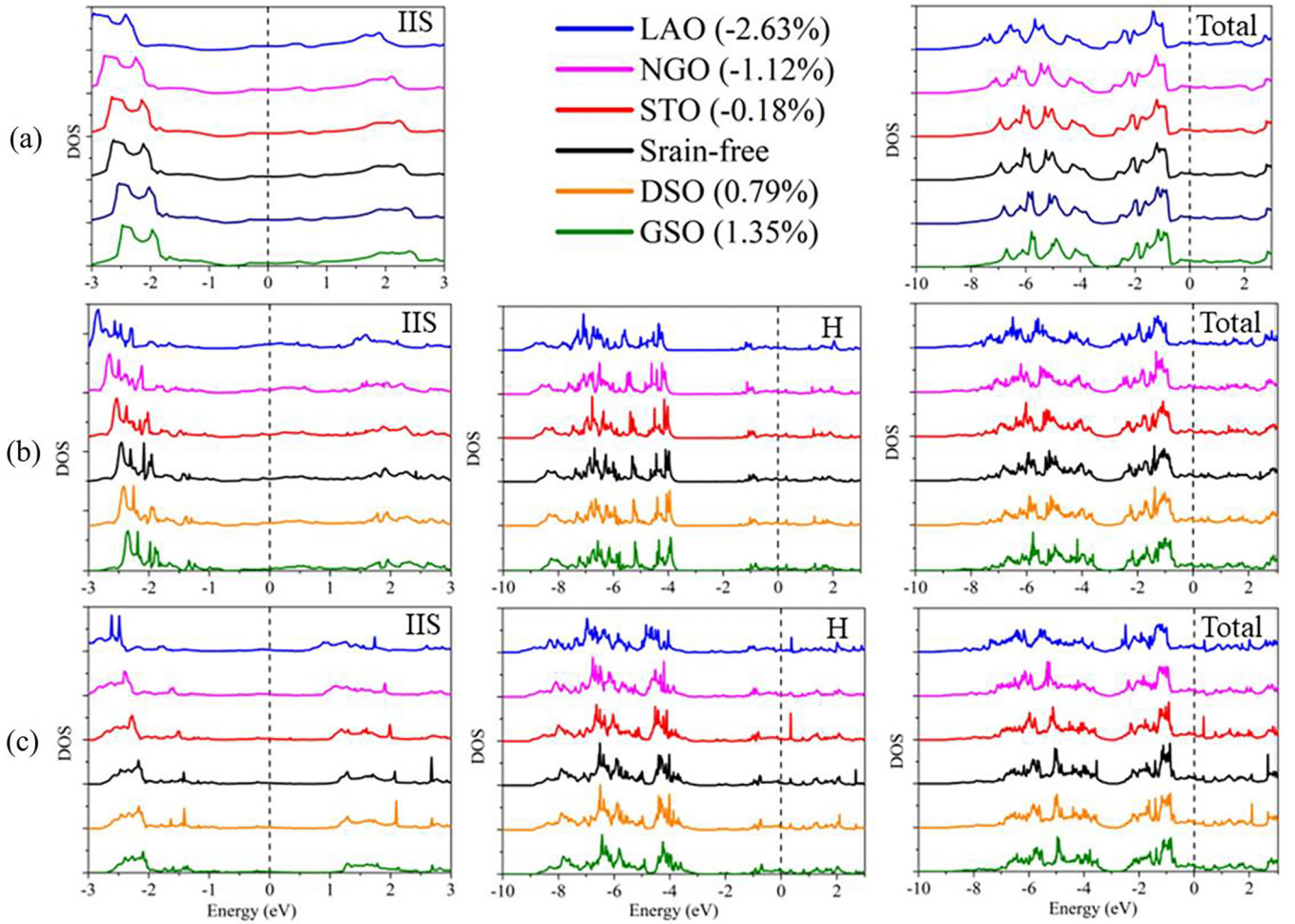


FIG. 3. Projected and total density of states in  $\text{NdNiO}_2\text{H}_x$  [(a)  $x = 0$ , (b)  $x = 0.25$ , and (c)  $x = 0.5$ ] under different strains. The Fermi level has been set to 0 eV.

under tensile strains (DSO and GSO in-plane strains), indicative of a  $p$ -type doping effect. The phenomenon that the strain shifts the relative energy positions of the bands has also been observed by Han and van Veenendaal [52] for  $\text{LaNiO}_3$ .

To better explore the electron-electron interaction in transition metal oxides, the influence of the Hubbard  $U$  parameter on the electronic structures of NNOH is considered. Figure S1 in the Supplemental Material [53] compares the

electronic structures of NNOH obtained by employing different Hubbard  $U$  values. Under  $U = 4$  eV, the Nd  $5d$  electron pocket around the  $\Gamma$  point is larger than that under  $U = 0$  eV due to different Coulomb repulsion. Additionally, the bands under  $U = 0$  eV exhibit a slight upward shift as compared with the case under  $U = 4$  eV, whereas the evolution of band structures and DOSs with H concentration is insensitive to Hubbard  $U$  values, i.e., our main conclusions are not influenced by the  $U$  parameter.

### C. Orbital filling and polarization of NNOH under different in-plane strains

To further study the Ni orbital occupation in NNOH under different strains, we calculate COHP to obtain the Mulliken GP of Ni  $3d$  orbitals. Mulliken GP can be used to estimate the electronic charge distribution in a material, similar to other methods like integrating DOS in VASP and Wannier functions to analyze orbital occupations in the literature [26]. Considering that there exist two chemical conditions around the Ni site, i.e.,  $\text{Ni}_2\text{O}_4$  (with IIS) and  $\text{Ni}_2\text{O}_4\text{H}_2$  (H occupying IIS) local environments, we calculate the Mulliken GPs of Ni  $3d$  orbitals under both local environments as well as the average value, as seen in Figs. 4(a)–4(d). The results show

TABLE I. The lattice parameters for NNO, LAO, LSAT/NGO, STO, DSO, and GSO. The positive and negative values of strain represent compressive and tensile strain applied on NNO, respectively. The Fermi energy corresponds to that of NNO under different strains.

	$ab$ (Å)	Strain	Fermi energy (eV)
NNO	3.912	–	6.36
LAO	3.809	–2.63%	6.85
LSAT/NGO	3.868	–1.12%	6.57
STO	3.905	–0.18%	6.39
DSO	3.943	0.79%	6.21
GSO	3.965	1.35%	6.10

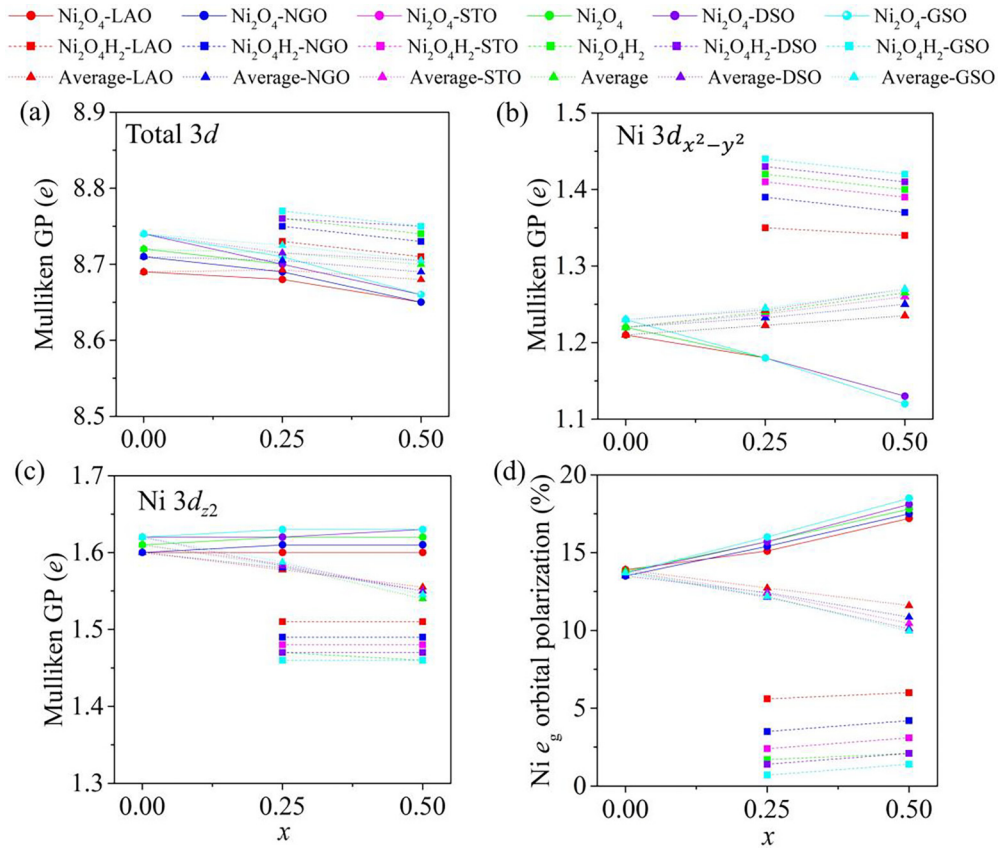


FIG. 4. Ni  $3d$  orbital occupations under  $\text{Ni}_2\text{O}_4$ ,  $\text{Ni}_2\text{O}_4\text{H}_2$  environment, and the averaged values as a function of H concentration under different strains. Mulliken gross population in (a) Ni  $3d$  orbital, (b) Ni  $3d_{x^2-y^2}$  orbital and (c) Ni  $3d_{z^2}$  orbital; (d) Ni  $e_g$  orbital polarization.

that, under certain strain, the filling of the Ni  $3d$  orbital decreases with increasing H concentration in all cases. This can be caused by two factors: on one hand, a loss of electrons in the Ni  $3d_{x^2-y^2}$  orbital is presented, while electron populations are almost unchanged in the Ni  $3d_{z^2}$  orbital for  $\text{Ni}_2\text{O}_4$  and  $\text{Ni}_2\text{O}_4\text{H}_2$  sites with increasing H concentration; on the other hand, in Figs. 2(b) and 2(c), there exists a bonding state around  $-2$  eV along  $Z$ - $R$ - $A$ - $Z$  path and an antibonding state crossing the Fermi level around the  $\Gamma$  point. This bonding-antibonding state formed by the H  $1s$  orbital hybridizing with the Ni  $3d_{z^2}$  orbital reduces the average occupation of the Ni  $3d_{z^2}$  orbital. The former causes the filling of the Ni  $3d$  orbital to decrease with increasing H concentration in both  $\text{Ni}_2\text{O}_4$  and  $\text{Ni}_2\text{O}_4\text{H}_2$  sites, and the latter results in the reduced average occupation of the Ni  $3d$  orbital with H concentration rising.

One can see from Fig. 4(b) that the strain influences the occupation of Ni  $3d_{x^2-y^2}$  in NNOH to some extent. Specifically, for the  $\text{Ni}_2\text{O}_4\text{H}_2$  site, the compressive strains (LAO, NGO, and STO in-plane strains) reduce the Mulliken GP, while the tensile strains (DSO and GSO in-plane strains) enhance it. For example, the Mulliken GP of Ni  $3d_{x^2-y^2}$  in the  $\text{Ni}_2\text{O}_4\text{H}_2$  site decreases from  $\sim 1.41 e$  to  $\sim 1.34 e$  and increases slightly from  $\sim 1.41 e$  to  $\sim 1.43 e$  under LAO and DSO in-plane strains, respectively. However, for the  $\text{Ni}_2\text{O}_4$  site, the difference in the filling of Ni  $3d_{x^2-y^2}$  between compressive and tensile strains can be negligible. In terms of Ni  $3d_{z^2}$  in NNOH, the influence of strain on the Mulliken GP for both  $\text{Ni}_2\text{O}_4$  and  $\text{Ni}_2\text{O}_4\text{H}_2$  sites is slight. For instance, with LAO in-plane strain applied,

the Mulliken GP of Ni  $3d_{z^2}$  in the  $\text{Ni}_2\text{O}_4$  ( $\text{Ni}_2\text{O}_4\text{H}_2$ ) site changes slightly from  $1.61$  ( $\sim 1.47$ )  $e$  to  $1.6$  ( $1.51$ )  $e$ . Similarly, with GSO in-plane strain applied, the Mulliken GP varies slightly from  $1.61$  ( $\sim 1.47$ )  $e$  to  $1.62$  ( $1.46$ )  $e$ . Consequently, there is a tiny change in the average value of the Ni  $3d_{z^2}$  occupation. Additionally, the Ni  $e_g$  orbital polarization  $P$  is calculated using the formula  $P = \frac{n_{3d_{z^2}} - n_{3d_{x^2-y^2}}}{n_{3d_{z^2}} + n_{3d_{x^2-y^2}}}$ . The average  $P$  decreases with increasing H concentration, indicative of an electron doping in the  $3d_{x^2-y^2}$  state, which makes the nickelates different from cuprates, for which the hole doping in the  $3d_{x^2-y^2}$  state is more suitable to realize much higher- $T_c$  superconductivity [54–56].

To further explore the difference in the orbital filling among Mulliken and Wannier methods, we also calculate the Ni  $3d$  filling from Wannier orbitals. Figure S3 in the Supplemental Material [53] shows orbital filling as a function of H concentration in  $\text{NdNiO}_2\text{H}_x$  obtained from Mulliken GP and Wannier orbitals. Although discrepancy exists between absolute values, the trends of Ni  $3d$  filling with H concentration using both methods are consistent. Considering that Wannier orbital calculations are computationally expensive, we only provide Mulliken GP results in this paper.

#### D. MLWF calculations

Generally, the hybridization between two orbitals can be estimated using two parameters: on-site energy difference

TABLE II. Hopping energy  $t$  and on-site energy difference  $\Delta$  (unit: eV) between different orbitals of  $\text{NdNiO}_2\text{H}_x$  ( $x = 0, 0.25, 0.5$ ) under different in-plane strains ( $t_1$  and  $\Delta_1$  corresponding to the parameter between the Ni  $d_{x^2-y^2}$  and O  $p$  orbitals;  $t_2$  and  $\Delta_2$  corresponding to the parameter between the interstitial  $s$  and O  $p$  orbitals;  $t_3$  and  $\Delta_3$  corresponding to the parameter between the Nd  $d_{xy}$  and O  $p$  orbitals; and  $t_4$  and  $\Delta_4$  corresponding to the parameter between the Nd  $d_{z^2}$  and O  $p$  orbitals).

Structure		Hopping energy				On-site energy difference			
		$t_1$	$t_2$	$t_3$	$t_4$	$\Delta_1$	$\Delta_2$	$\Delta_3$	$\Delta_4$
NdNiO <sub>2</sub> H <sub>x</sub> without strain	$x = 0$	1.31	0.69	0.07	-0.04	4.09	6.68	7.59	7.46
	$x = 0.25$	-1.17	0	0	0.02	3.87	-	7.35	6.26
	$x = 0.5$	-1.16	0	0	0	3.83	-	7.20	6.19
NdNiO <sub>2</sub> H <sub>x</sub> <sup>STO</sup>	$x = 0$	1.32	0.70	0.06	-0.04	4.10	6.70	7.61	7.48
	$x = 0.25$	-1.20	0	0	0	3.93	-	7.1	6.34
	$x = 0.5$	-1.20	0	0	0	2.77	-	7.3	6.26
NdNiO <sub>2</sub> H <sub>x</sub> <sup>LAO</sup>	$x = 0$	1.45	0.66	0.06	-0.04	4.33	7.02	7.90	7.85
	$x = 0.25$	-1.34	0	0	0	4.16	-	7.71	6.57
	$x = 0.5$	-1.33	0	0	0	4.16	-	7.56	6.51
NdNiO <sub>2</sub> H <sub>x</sub> <sup>NGO</sup>	$x = 0$	1.37	0.68	0.06	-0.04	4.18	6.82	7.72	7.62
	$x = 0.25$	-1.25	0	0	0	4.02	-	7.54	6.43
	$x = 0.5$	-1.25	0	0	0	4.01	-	7.40	6.36
NdNiO <sub>2</sub> H <sub>x</sub> <sup>GSO</sup>	$x = 0$	1.25	0.67	0.07	-0.02	3.94	6.51	7.42	7.25
	$x = 0.25$	-1.12	0	0	0	3.77	-	7.21	6.17
	$x = 0.5$	-1.12	0	0	0	3.73	-	7.09	6.13
NdNiO <sub>2</sub> H <sub>x</sub> <sup>DSO</sup>	$x = 0$	1.31	0.44	-0.02	-0.02	3.94	7.61	7.42	7.33
	$x = 0.25$	-1.15	0	0	0	3.84	-	7.30	6.23
	$x = 0.5$	-1.15	0	0	0	3.81	-	7.18	6.19

$\Delta$  and hopping integral  $t$  [57]. Hence, we perform MLWF calculations to obtain these two parameters to explore the hybridization between different orbitals in NNOH, as summarized in Table II. Previous studies have reported that the hybridization between Ni  $3d_{x^2-y^2}$  and R  $d$  orbitals in NNO is very weak [58,59]. However, in Table II, we find that, under certain strain, the indirect hopping between Ni  $3d_{x^2-y^2}$  and IIS orbitals via the O  $p$  orbital in NNO is unexpectedly large, suggesting that the hybridization between the Ni  $3d_{x^2-y^2}$  orbital and itinerant electrons in the Nd spacer layer is strong, which is consistent with recent literature [26,60]. The corresponding hopping path is plotted in Fig. 5. Additionally, the on-site energy difference between IIS and O  $p$  orbitals

(6.51–7.02 eV) is smaller than that between Nd  $d_{xy}/d_{z^2}$  and O  $p$  orbitals (7.42–7.90 eV) in NNO under most strains, which further confirms that the Ni  $3d_{x^2-y^2}$  orbital has significant coupling with the IIS orbital, substantially stronger than that with Nd  $d$  orbitals. In terms of NNO under DSO strain, although the on-site energy difference between IIS and O  $p$  orbitals (7.61 eV) is 0.19/0.28 eV larger than that between Nd  $d_{xy}/d_{z^2}$  and O  $p$  orbitals (7.42/7.33 eV), the dominated large hopping integral between IIS and O  $p$  orbitals (0.44 eV) leads to the strong hybridization. For cuprates, large on-site energy difference  $\Delta_{dp}$  between Cu  $3d_{x^2-y^2}$  and O  $2p$  orbitals suppresses the superconductivity [61]. Considering that  $\Delta_1$  of  $\sim 4$  eV in nickelates, as shown in Table II, is larger than that of  $\sim 2$  eV in cuprates [16], it can be explained that  $T_c$  in nickelates ( $\sim 15$  K) is lower than that in cuprates ( $> 30$  K).

As H is introduced, the hopping path to the IIS orbital in the  $\text{Ni}_2\text{O}_4\text{H}_2$  site is diminished. In this case, the hopping path  $t_2$  in Fig. 5 is replaced by  $t'_2$ , which causes the  $t_2$  to be reduced to zero under each strain, as seen in Table II. Moreover, it can be noted that the compressive strain enhances  $t_1$ , especially for the case under LAO strain, which is in line with the increased bandwidth of Ni  $3d_{x^2-y^2}$  in Fig. 4 and implies that LAO strain may have a significant impact on the superconductivity of nickelates. On the other hand, the tensile strain reduces  $t_1$ . It should be noted that 2D-like electronic structure of the infinite layer is believed to be beneficial to superconductivity [26], which also mimics the situation in cuprates [62]. With H doping, the interlayer hopping related to IIS orbitals is eliminated, resulting in more 2D-like electronic structure. However, as the H concentration rises, the increasing Ni  $e_g$  orbital polarization enhances the Ni  $3d$  orbital mixing, as shown in Fig. 4(d), which is in competition with decreased interlayer hopping and might transform the electronic structure back to be more

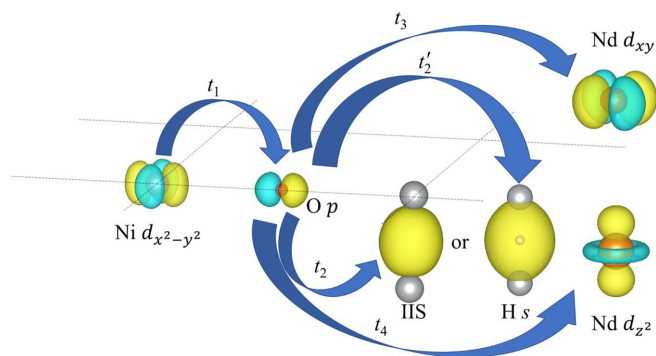


FIG. 5. The hopping path in  $\text{NdNiO}_2\text{H}_x$  ( $x = 0, 0.25, 0.5$ ).  $t_1$ : Ni  $3d_{x^2-y^2} \rightarrow \text{O}2p$ ;  $t_2$ :  $\text{O}2p \rightarrow$  itinerant interstitial  $s$  (IIS);  $t'_2$ :  $\text{O}2p \rightarrow \text{H}s$ ;  $t_3$ :  $\text{O}2p \rightarrow \text{Nd}d_{xy}$ ;  $t_4$ :  $\text{O}2p \rightarrow \text{Nd}d_{z^2}$ . For  $\text{Ni}_2\text{O}_4$  site, the  $t_2$  represents the path from the O  $p$  to the IIS orbital; for  $\text{Ni}_2\text{O}_4\text{H}_2$  site, the  $t_2$  is replaced by  $t'_2$ , which represents the path from the O  $p$  to the H  $s$  orbital.

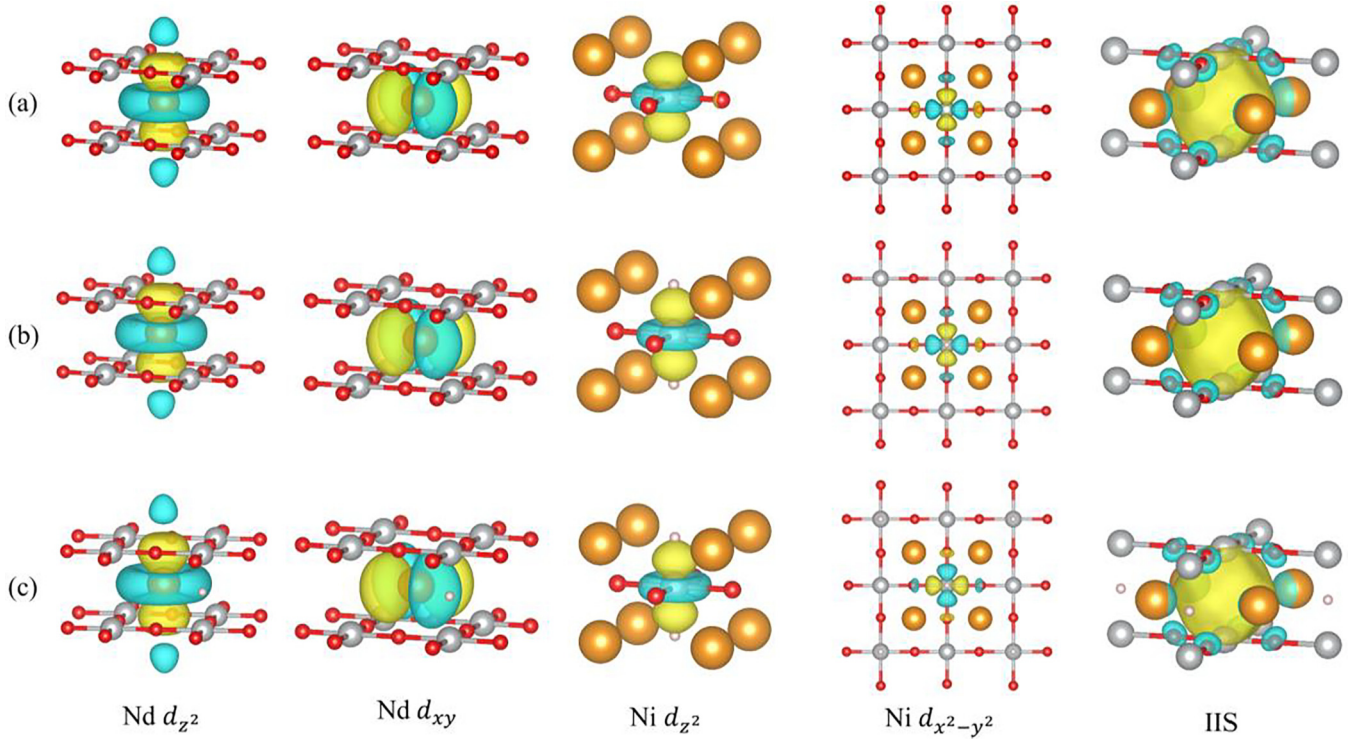


FIG. 6. Isovalue surfaces of Nd  $d_{z^2}$ , Nd  $d_{xy}$ , Ni  $d_{z^2}$ , Ni  $d_{x^2-y^2}$ , and itinerant interstitial  $s$  (IIS) orbitals for strain-free NdNiO<sub>2</sub>H<sub>*x*</sub> [(a)  $x = 0$ , (b)  $x = 0.25$ , and (c)  $x = 0.5$ ]. The orange, gray, red, and white atoms represent Nd, Ni, O, and H, respectively. The yellow and light blue areas represent positive and negative values, respectively. All the isosurface levels are set to 0.5.

three-dimensional (3D)-like. This might be relevant for the observed superconductivity within a very narrow H-doping window of  $0.22 \leq x \leq 0.28$  [26].

The isovalue surfaces of MLWFs for different projected orbitals in NNOH without strain are explicitly shown in Figs. 6(a)–6(c). Each orbital has the same size and shape under different H concentration, suggesting that these projected orbitals are insensitive to the H concentrations, i.e., the effect caused by the H insertion is relatively local. Additionally, the isovalue surfaces for NNOH under different strains are provided in Fig. S2 in the Supplemental Material [53]. The results show that the strain also has negligible effects on these isovalue surfaces.

Additionally, to better understand the role of Sr in the superconductivity of nickelate, we calculate the Ni  $3d_{x^2-y^2}$ - $3d_{z^2}$  orbital polarization ( $I_{OP}$ ) and the orbital hybridization between Ni  $3d_{x^2-y^2}$  and IIS orbitals with 11 Wannier projectors (5 Nd  $d$  orbitals, 5 Ni  $d$  orbitals, and an IIS orbital) in Nd<sub>1-*x*</sub>Sr<sub>*x*</sub>NiO<sub>2</sub> ( $x = 0, 0.05, 0.1, 0.15, 0.2$ ), which have been observed in the experiments via resonant inelastic x-ray scattering and x-ray absorption spectroscopy and were proposed to be strongly related with the superconductivity in nickelates [26]. The results summarized in Table S1 in the Supplemental Material [53] show that  $t_6$  and  $I_{OP}$  under different Sr concentrations are almost unchanged, suggesting that the doped Sr has negligible effects on  $t_6$  and  $I_{OP}$ . Therefore, we conclude that the H concentration and in-plane strains influence the hybridization between Ni  $d_{x^2-y^2}$  and Nd-layer orbitals to some extent, while Sr doping affects the hopping intensity ( $t_6 - t_8$ ) and Ni  $e_g$  orbital polarization slightly.

#### IV. CONCLUSIONS

In this paper, we systematically study the electronic structures and hybridization between different orbitals in NdNiO<sub>2</sub>H<sub>*x*</sub> ( $x = 0, 0.25, 0.5$ ) under different in-plane strains. The results show that, with H introduced, the band structure of Ni  $3d_{x^2-y^2}$  shifts to lower energy accompanied by the enhanced filling of the Ni  $3d_{x^2-y^2}$  orbital, suggesting an  $n$ -type doping effect in the Ni  $3d_{x^2-y^2}$  orbital. With the increasing H concentration, the IIS band near the Fermi level gradually decreases and eventually disappears at  $x = 0.5$ . Meanwhile, the interlayer hopping related to IIS orbitals is also reduced, resulting in more 2D-like electronic structure, which competes with the enhanced Ni  $3d$  orbital mixing and might suppress the superconductivity. With compressive strain applied, the bandwidth of the Ni  $3d_{x^2-y^2}$  orbital increases, indicative of the stronger effective Ni  $3d_{x^2-y^2}$  nearest-neighbor hopping. In addition, the large on-site energy difference  $\Delta_{dp}$  of  $\sim 4$  eV between Ni  $3d_{x^2-y^2}$  and O  $2p$  orbitals explains the lower  $T_c$  in nickelates ( $\sim 15$  K) as compared with the case in cuprates, whereas the H concentration and strain have slight influences on the isovalue surfaces of projected orbitals, PDOSs for IIS and H  $s$  orbitals, and TDOSs. Additionally, it is found that the electronic properties of NNO without strain are almost not affected by Sr concentration (0–20%) and Hubbard  $U$  value.

#### ACKNOWLEDGMENT

This paper was supported by the Key Research and Development Program from the Ministry of Science and

Technology (Grant No. 2023YFA1406301), National Natural Science Foundation of China (Grant No. 12274061), and Joint Funds of the National Natural Science Foundation of China (Grant No. U1930120). The authors

acknowledge Hefei Advanced Computing Center for providing high-performance computing resources that have contributed to the research results reported within this paper.

- 
- [1] J. G. Bednorz and K. A. Müller, *Z. Phys. B: Condens. Matter* **64**, 189 (1986).
- [2] J. Bardeen, L. N. Cooper, and J. R. Schrieffer, *Phys. Rev.* **106**, 162 (1957).
- [3] M. Francois, A. Junod, K. Yvon, A. Hewat, J. Capponi, P. Strobel, M. Marezio, and P. Fischer, *Solid State Commun.* **66**, 1117 (1988).
- [4] M. Smith, A. Manthiram, J. Zhou, J. Goodenough, and J. Markert, *Nature (London)* **351**, 549 (1991).
- [5] M. Azuma, Z. Hiroi, M. Takano, Y. Bando, and Y. Takeda, *Nature (London)* **356**, 775 (1992).
- [6] D. Li, K. Lee, B. Y. Wang, M. Osada, S. Crossley, H. R. Lee, Y. Cui, Y. Hikita, and H. Y. Hwang, *Nature (London)* **572**, 624 (2019).
- [7] B. Cheng, D. Cheng, K. Lee, L. Luo, Z. Chen, Y. Lee, B. Wang, M. Mootz, I. Perakis, Z. Shen *et al.*, *Nat. Mater.* **23**, 775 (2024).
- [8] C. T. Parzyck, N. K. Gupta, Y. Wu, V. Anil, L. Bhatt, M. Bouliane, R. Gong, B. Z. Gregory, A. Luo, R. Sutarto *et al.*, *Nat. Mater.* **23**, 486 (2024).
- [9] H. Qi, X. Han, X. Sui, B. Huang, H. Xiao, and L. Qiao, *ACS Appl. Mater. Interfaces* **16**, 10924 (2024).
- [10] M. Xu, Y. Zhao, X. Ding, H. Leng, S. Zhang, J. Gong, H. Xiao, X. Zu, H. Luo, K.-J. Zhou *et al.*, *Front. Phys.* **19**, 33209 (2024).
- [11] X. Sui, X. Han, H. Jin, X. Wu, L. Qiao, X. Shao, and B. Huang, *Phys. Rev. B* **109**, 155156 (2024).
- [12] X. Han, P. Li, X. Sui, H. Jin, F. Luo, L. Qiao, and B. Huang, *Phys. Rev. B* **108**, 165145 (2023).
- [13] V. V. Poltavets, K. A. Lokshin, S. Dikmen, M. Croft, T. Egami, and M. Greenblatt, *J. Am. Chem. Soc.* **128**, 9050 (2006).
- [14] J. Hao, X. Fan, Q. Li, X. Zhou, C. He, Y. Dai, B. Xu, X. Zhu, and H.-H. Wen, *Phys. Rev. B* **103**, 205120 (2021).
- [15] P. Worm, L. Si, M. Kitatani, R. Arita, J. M. Tomczak, and K. Held, *Phys. Rev. Mater.* **6**, L091801 (2022).
- [16] A. S. Botana and M. R. Norman, *Phys. Rev. X* **10**, 011024 (2020).
- [17] Y. Zhang, L.-F. Lin, W. Hu, A. Moreo, S. Dong, and E. Dagotto, *Phys. Rev. B* **102**, 195117 (2020).
- [18] A. S. Botana and M. R. Norman, *Phys. Rev. Mater.* **2**, 104803 (2018).
- [19] B. H. Goodge, D. Li, K. Lee, M. Osada, B. Y. Wang, G. A. Sawatzky, H. Y. Hwang, and L. F. Kourkoutis, *Proc. Natl. Acad. Sci. USA* **118**, e2007683118 (2021).
- [20] Z. Chen, M. Osada, D. Li, E. M. Been, S.-D. Chen, M. Hashimoto, D. Lu, S.-K. Mo, K. Lee, B. Y. Wang *et al.*, *Matter* **5**, 1806 (2022).
- [21] J. Zaanen, G. A. Sawatzky, and J. W. Allen, *Phys. Rev. Lett.* **55**, 418 (1985).
- [22] M. Hepting, D. Li, C. J. Jia, H. Lu, E. Paris, Y. Tseng, X. Feng, M. Osada, E. Been, Y. Hikita *et al.*, *Nat. Mater.* **19**, 381 (2020).
- [23] B. H. Goodge, B. Geisler, K. Lee, M. Osada, B. Y. Wang, D. Li, H. Y. Hwang, R. Pentcheva, and L. F. Kourkoutis, *Nat. Mater.* **22**, 466 (2023).
- [24] Y. Zhang, J. Zhang, X. He, J. Wang, and P. Ghosez, *PNAS Nexus* **2**, pgad108 (2023).
- [25] L. Si, W. Xiao, J. Kaufmann, J. M. Tomczak, Y. Lu, Z. Zhong, and K. Held, *Phys. Rev. Lett.* **124**, 166402 (2020).
- [26] X. Ding, C. C. Tam, X. Sui, Y. Zhao, M. Xu, J. Choi, H. Leng, J. Zhang, M. Wu, H. Xiao *et al.*, *Nature (London)* **615**, 50 (2023).
- [27] Y. Zhang, L.-F. Lin, A. Moreo, T. A. Maier, and E. Dagotto, *Phys. Rev. B* **109**, 045151 (2024).
- [28] G. A. Pan, D. F. Segedin, H. LaBollita, Q. Song, E. M. Nica, B. H. Goodge, A. T. Pierce, S. Doyle, S. Novakov, D. C. Carrizales *et al.*, *Nat. Mater.* **21**, 160 (2022).
- [29] K. Lee, B. Y. Wang, M. Osada, B. H. Goodge, T. C. Wang, Y. Lee, S. Harvey, W. J. Kim, Y. Yu, C. Murthy *et al.*, *Nature* **619**, 288 (2022).
- [30] Q. Gao, S. Fan, Q. Wang, J. Li, X. Ren, I. Bialo, A. Drewanowski, P. Rothenbühler, J. Choi, Y. Wang *et al.*, [arXiv:2208.05614](https://arxiv.org/abs/2208.05614).
- [31] P. Hohenberg and W. Kohn, *Phys. Rev.* **136**, B864 (1964).
- [32] W. Kohn and L. J. Sham, *Phys. Rev.* **140**, A1133 (1965).
- [33] G. Kresse and J. Furthmüller, *Phys. Rev. B* **54**, 11169 (1996).
- [34] G. Kresse and D. Joubert, *Phys. Rev. B* **59**, 1758 (1999).
- [35] J. P. Perdew, K. Burke, and M. Ernzerhof, *Phys. Rev. Lett.* **77**, 3865 (1996).
- [36] H. J. Monkhorst and J. D. Pack, *Phys. Rev. B* **13**, 5188 (1976).
- [37] Y. Nomura, M. Hirayama, T. Tadano, Y. Yoshimoto, K. Nakamura, and R. Arita, *Phys. Rev. B* **100**, 205138 (2019).
- [38] N. Marzari, A. A. Mostofi, J. R. Yates, I. Souza, and D. Vanderbilt, *Rev. Mod. Phys.* **84**, 1419 (2012).
- [39] A. A. Mostofi, J. R. Yates, Y.-S. Lee, I. Souza, D. Vanderbilt, and N. Marzari, *Comput. Phys. Commun.* **178**, 685 (2008).
- [40] Z. He and A. J. Millis, *Phys. Rev. B* **91**, 195138 (2015).
- [41] D. F. Segedin, B. H. Goodge, G. A. Pan, Q. Song, H. LaBollita, M.-C. Jung, H. El-Sherif, S. Doyle, A. Turkiewicz, N. K. Taylor *et al.*, *Nat. Commun.* **14**, 1468 (2023).
- [42] X. Ren, J. Li, W.-C. Chen, Q. Gao, J. J. Sanchez, J. Hales, H. Luo, F. Rodolakis, J. L. McChesney, T. Xiang *et al.*, *Commun. Phys.* **6**, 341 (2023).
- [43] Z. Liu, C. Xu, C. Cao, W. Zhu, Z. F. Wang, and J. Yang, *Phys. Rev. B* **103**, 045103 (2021).
- [44] E. Been, W.-S. Lee, H. Y. Hwang, Y. Cui, J. Zaanen, T. Devereaux, B. Moritz, and C. Jia, *Phys. Rev. X* **11**, 011050 (2021).
- [45] H. J. Xiang, S.-H. Wei, and M.-H. Whangbo, *Phys. Rev. Lett.* **100**, 167207 (2008).
- [46] R. Dronskowski and P. E. Blöchl, *J. Phys. Chem.* **97**, 8617 (1993).
- [47] V. L. Deringer, A. L. Tchougréeff, and R. Dronskowski, *J. Phys. Chem. A* **115**, 5461 (2011).
- [48] R. S. Mulliken, *J. Chem. Phys.* **23**, 1833 (1955).
- [49] D. Kutsuzawa, Y. Hirose, A. Chikamatsu, S. Nakao, Y. Watahiki, I. Harayama, D. Sekiba, and T. Hasegawa, *Appl. Phys. Lett.* **113**, 253104 (2018).

- [50] T. Yajima, A. Kitada, Y. Kobayashi, T. Sakaguchi, G. Bouilly, S. Kasahara, T. Terashima, M. Takano, and H. Kageyama, *J. Am. Chem. Soc.* **134**, 8782 (2012).
- [51] C. Zhao, B. Luo, and C. Chen, *RSC Adv.* **7**, 19492 (2017).
- [52] M. J. Han and M. van Veenendaal, *Phys. Rev. B* **84**, 125137 (2011).
- [53] See Supplemental Material at <http://link.aps.org/supplemental/10.1103/PhysRevMaterials.8.064802> for additional orbital and electronic characterization.
- [54] B. Keimer, S. A. Kivelson, M. R. Norman, S. Uchida, and J. Zaanen, *Nature (London)* **518**, 179 (2015).
- [55] P. A. Lee, N. Nagaosa, and X.-G. Wen, *Rev. Mod. Phys.* **78**, 17 (2006).
- [56] N. P. Armitage, P. Fournier, and R. L. Greene, *Rev. Mod. Phys.* **82**, 2421 (2010).
- [57] P. Jiang, L. Si, Z. Liao, and Z. Zhong, *Phys. Rev. B* **100**, 201106(R) (2019).
- [58] X. Wu, D. Di Sante, T. Schwemmer, W. Hanke, H. Y. Hwang, S. Raghu, and R. Thomale, *Phys. Rev. B* **101**, 060504(R) (2020).
- [59] G.-M. Zhang, Y.-f. Yang, and F.-C. Zhang, *Phys. Rev. B* **101**, 020501(R) (2020).
- [60] Y. Gu, S. Zhu, X. Wang, J. Hu, and H. Chen, *Commun. Phys.* **3**, 84 (2020).
- [61] C. Weber, K. Haule, and G. Kotliar, *Phys. Rev. B* **82**, 125107 (2010).
- [62] H. Sakakibara, H. Usui, K. Kuroki, R. Arita, and H. Aoki, *Phys. Rev. Lett.* **105**, 057003 (2010).